

Article

Spatiotemporal Features and Time-Lagged Effects of Drought on Terrestrial Ecosystem in Southwest China

Pan Jiang ^{1,†}, Yuxi Wang ^{2,†} , Yang Yang ^{3,4} , Xinchun Gu ^{5,6} , Yi Huang ³, Lei Liu ^{7,*} and Liang Liu ^{1,*}

- ¹ School of Economics and Management, Southwest University of Science and Technology, Mianyang 621010, China; jiangpan@mails.swust.edu.cn
- ² Chongqing Key Laboratory of Surface Process and Environment Remote Sensing in the Three Gorges Reservoir Area, Chongqing Normal University, Chongqing 401331, China; 2021110514068@stu.cqnu.edu.cn
- ³ School of Sciences, Tibet University, Lhasa 850000, China; yangyang1hh@163.com (Y.Y.); hyhy1232021@163.com (Y.H.)
- ⁴ State Key Laboratory of Tibetan Plateau Earth System, Environment and Resources (TPESER), Institute of Tibetan Plateau Research, Chinese Academy of Sciences, Beijing 100101, China
- ⁵ State Key Laboratory of Hydraulic Engineering Simulation and Safety, School of Civil Engineering, Tianjin University, Tianjin 300072, China; gxc@tju.edu.cn
- ⁶ State Key Laboratory of Simulation and Regulation of Water Cycle in River Basin, China Institute of Water Resources and Hydropower Research, Beijing 100044, China
- ⁷ College of Life Science and Biotechnology, Mianyang Normal University, Mianyang 621000, China
- * Correspondence: liulei@mnu.cn (L.L.); liuliang@swust.edu.cn (L.L.)
- † These authors contributed equally to this work.

Abstract: With global warming, the increase in the frequency and intensity of droughts have severely affected the balance of terrestrial ecosystems. Although the immediate effects of drought on vegetation growth have been widely studied, the time-lagged effects have been neglected, particularly in ecologically fragile karst areas. We examined the vegetation growth trends and abrupt changes in southwest China from 1990 to 2018 by reconstructing the normalized difference vegetation index (NDVI); we then used the standardized precipitation and evapotranspiration index (SPEI) to explore the drought evolution characteristics and the time-lagged effect of drought on vegetation growth. The results showed that 97% of the study area exhibited a greening trend, which accelerated after 1995. Spring drought increased noticeably. We demonstrated that drought had a time-lagged effect on vegetation growth; 27.28% of the vegetation lands had a lag time of less than 3 months, and the mean lagged time in karst areas was shorter than that in non-karst areas. Compared to other vegetation types, the cultivated vegetation had weaker drought resistance, while the mixed-forest had stronger tolerance to drought. This study contributes to a further understanding of the drought–vegetation relationship and has important implications for optimizing vegetation conservation strategies in southwest China while coping with climate change.

Keywords: EEMD; BFAST; vegetation; NDVI; drought; time-lagged effect; southwest China



Citation: Jiang, P.; Wang, Y.; Yang, Y.; Gu, X.; Huang, Y.; Liu, L.; Liu, L. Spatiotemporal Features and Time-Lagged Effects of Drought on Terrestrial Ecosystem in Southwest China. *Forests* **2023**, *14*, 781. <https://doi.org/10.3390/f14040781>

Academic Editor: Martin D. Venturas

Received: 10 March 2023

Revised: 3 April 2023

Accepted: 7 April 2023

Published: 10 April 2023



Copyright: © 2023 by the authors. Licensee MDPI, Basel, Switzerland. This article is an open access article distributed under the terms and conditions of the Creative Commons Attribution (CC BY) license (<https://creativecommons.org/licenses/by/4.0/>).

1. Introduction

Vegetation, as a producer of terrestrial ecosystems, is the fundamental link that connects soil, water, and atmosphere, playing an irreplaceable role in regulating energy exchange, the terrestrial carbon cycle, and climate change [1]. As such, understanding the vegetation dynamics and growth trends over a long time series is important for monitoring terrestrial ecosystem changes as well as sustainable development. However, it is hard to accurately quantify the large-scale vegetation evolution process and characteristics by traditional methods under the complex interaction of multiple factors, such as climate change, natural calamities, and human activities [2–4]. With the rapid development of remote sensing technology, multi-temporal remote sensing images have been widely used to detect vegetation cover changes. The satellite-based normalized difference vegetation

index (NDVI) can accurately represent the metabolic intensity of vegetation through red and near-infrared reflection data, which has been identified as a common index to evaluate vegetation activity [5,6]. However, with atmospheric disturbances, cloud cover, and sensor failures making the NDVI time series heavily noisy, as well as a lack of evidence from long-term field observations, the efficiency of NDVI in monitoring long-term changes in vegetation phenology still needs further exploration [7].

As a result of fertilization effects from increased CO₂ concentrations [8] and the implementation of effective land management policies [9], recent studies have determined that one-third of the global vegetation has been turning green since the early 1980s [10], and the NDVI at mid- and high-latitudes has improved significantly [11]. However, on the other hand, owing to intensified extreme climate change and continued agricultural expansion, some studies also show that global vegetation resilience has clearly declined since the early 2000s, and the greening trend is weaker in the southern hemisphere than in the northern hemisphere [12,13]. Many regions, such as equatorial rainforests, northern Eurasia and the southwestern United States, might have reversed their long-term greening, and even large-scale vegetation browning trends have occurred [14–16].

Although it remains controversial whether terrestrial net primary productivity has declined, these studies consistently show significantly different greening trends across regions. Studies for vegetation trends based on a single linear regression would likely enable vegetation browning to be overshadowed by overall vegetation greening. To overcome this problem, several methods have been proposed for detecting trend mutations, such as Landsat-based detection of Trends (LandTrendr) [17], the Vegetation Change Tracker (VCT) [18], the Breaks for Additive Seasonal and Trend (BFAST) algorithm [19], and the Detecting Breakpoints and Estimating Segments in Trend (DBEST) algorithm [20]. Among these, the BFAST algorithm allows the detection of abrupt changes in successive years of a time series NDVI, estimates the number, timing and magnitude of breakpoints per pixel, and has been widely used to monitor vegetation changes caused by forest disturbance and restoration [21,22]. However, outliers, seasonality and noise in the long time-series NDVI used for detection are usually neglected, which can influence the breakpoint detection results [23]. Ensemble Empirical Mode Decomposition (EEMD), as an adaptive method, can separate nonlinear and non-smooth physical components from signal sequences and its effectiveness has been proven [24–26].

Drought, the most economically destructive natural disaster of the 21st century, increases tree mortality [27], alters above- and below-ground carbon processes [28], and causes agricultural yield reductions [29]. Under the background of global warming, the frequency and severity of drought are increasing, which seriously threatens the global ecosystem balance [30]. A comprehensive understanding of the spatiotemporal characteristics and effect on vegetation of drought can contribute to drought mitigation and adaptation. However, it has been noticed that the effects of a drought event on vegetation growth do not appear immediately. The phenomenon where current vegetation growth is influenced by earlier water shortages is generally referred to as the time-lagged effect [31,32]. Wei et al. [33] found that drought had a time-lagged effect of 88.37% of the global grassland. However, the time and the intensity of time-lagged effects varies across vegetation types and range; the time-lag effect of drought occurs within 2 to 3 months on loess plateau grasslands [34] but can last 1–4 years in temperate and boreal forests [35]. Although many studies have been conducted on the lagging effects of global temperate habitats and grassland, research using remotely sensed vegetation data and understanding of subtropical and other vegetation-type zones are still limited.

In the past two decades, with large-scale afforestation and natural restoration, southwest China has become a hotspot for the “greening” of global vegetation cover, and it is the largest terrestrial carbon sink in China [36,37]. Furthermore, this area is the largest continuous karst landscape distribution region in the world; the area of karst is over 3×10^5 km² and is equal to one-quarter of the entire karst area in China, which makes the region vulnerable to seasonal droughts [38]. Ecological degradation represented by rock desertification

has become the biggest obstacle to regional social development [39]. Owing to severe soil erosion and low environmental capacity, it is difficult for the vegetation in this area to recover naturally after an extreme drought event [40]. In the future, with the drought center shifting to the south [41], southwest China will suffer from more frequent drought events. Although studies have been conducted to analyze the response of vegetation to drought and the resilience after drought events in the region, there are few studies on the lagged response of different vegetation types in karst and non-karst areas. Therefore, understanding vegetation evolution trends and their lagged response to drought in the southwest is important for formulating suitable policies for karst ecological restoration and actively responding to the ecological crisis brought about by global climate changes. In this study, we aimed to (1) detect the spatiotemporal evolutionary trends of vegetation in southwest China and when and where the abrupt changes occurred from NDVI extracted by EEMD; (2) compare the time-lagged effect of drought on different vegetation types in karst and non-karst areas.

2. Materials and Methods

2.1. Study Area

The study area in southwest China (20° – 35° N, 96° – 113° E) is composed of five provinces (municipalities and autonomous region), i.e., Sichuan, Yunnan, Guangxi, Guizhou, and Chongqing, covering an area of 1.37 million km^2 (Figure 1). The elevation ranges from -20 m to 6304 m, gradually declining from northwest to southeast. The area is dominated by a subtropical monsoon climate, characterized by rain and heat in the same period, and the mean annual rainfall is above 1100 mm [42]. The main vegetation types are coniferous forest, broad-leaved forest, mixed forest, grassland, shrub, alpine vegetation, and cultivated vegetation. However, as one of the largest contiguous karst regions in the world, southwest China is characterized by a fragile ecological environment [43], which makes the vegetation growth in the region more vulnerable to meteorological drought.

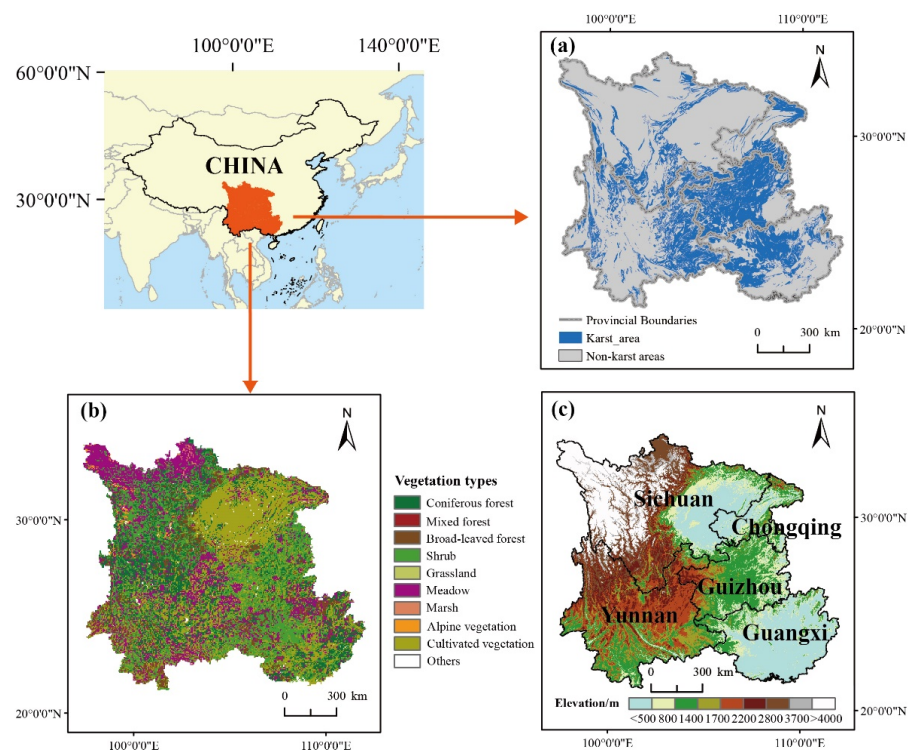


Figure 1. Location of the study area. (a) The spatial distribution of karst and non-karst areas; (b) vegetation type; (c) elevation.

2.2. Data

Commonly used NDVI datasets include the SPOT-VGT NDVI, the GIMMS3g NDVI, the AVHRR NDVI and the MODIS NDVI. The time series of the GIMMS3g NDVI dataset is longer (from July 1981 to December 2015) but data from the past 3 years are lacking and their resolution is low (8 km). The spatial resolution of SPOT-VGT and MODIS NDVI is high (approximately 1 km), but the time series is short, covering only approximately 20 years. The raw NDVI dataset selected for this study was provided by the NOAA Climate Data Record (CDR) of the AVHRR NDVI product, which is a daily product [44]. To reduce the influence of clouds, atmosphere, and solar altitude angle, the maximum value composite method was performed by using the rgee package in R from the Google Earth Engine platform to obtain monthly NDVI [45]. Then, the terra package was called for band fusion and cropping. We finally acquired a long-term series NDVI of the study area with a resolution of 5 km, covering the period 1990–2018. The dataset was taken from the National Science & Technology Infrastructure database of the National Earth System Science Data Center of China (<http://www.geodata.cn>, accessed on 3 October 2022). To ensure the consistency and accuracy of the 29-year AVHRR NDVI dataset, the raw MODIS and AVHRR NDVI datasets (2000–2018) were fitted by linear regression methods [46,47]. The results of the intercomparison of values and interannual trends between the AVHRR and MODIS NDVI datasets were mapped to slopes and correlation coefficients (r), which showed good agreement in magnitude and trend (Figure 2). The MODIS product used for validation during 2000–2018 was provided by the International Scientific and Technical Data Mirror Site, Computer Network Information Center, Chinese Academy of Sciences (<http://www.gscloud.cn>, accessed on 7 October 2022).

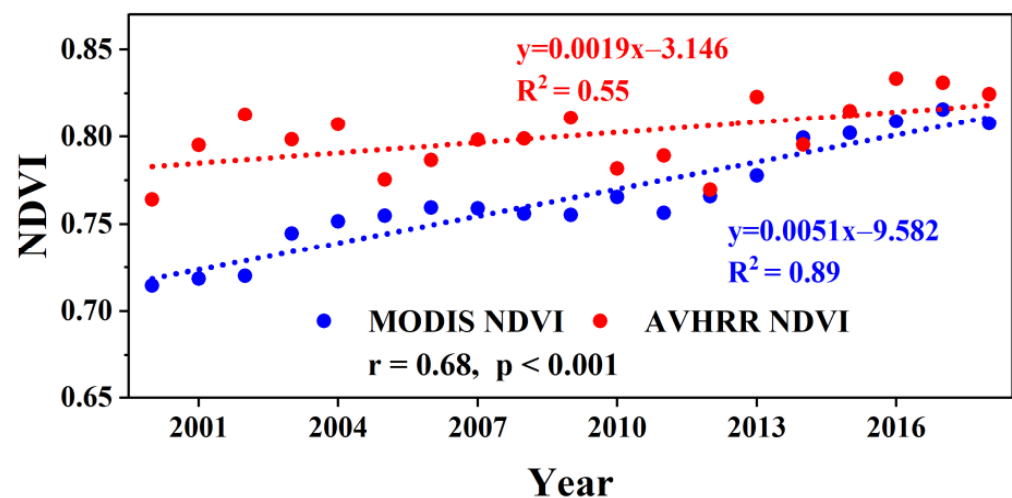


Figure 2. The intercomparison of the accuracy and consistency between the AVHRR and MODIS NDVI datasets during the overlapped period.

We acquired two meteorological datasets [48] with a spatial resolution of 1 km, including precipitation and potential evapotranspiration (PET), provided by the National Tibetan Plateau Data Center, Chinese Academy of Sciences (<http://data.tpdac.ac.cn/zh-hans/>, accessed on 14 October 2022). The precipitation datasets were generated by the Delta spatial downscaling scheme from the global 0.5° climate data of the Climate Research Unit and the global high-resolution climate data of WorldClim [49]. Using data from 496 independent meteorological observation stations across China for validation, the results were credible. The PET was estimated by the Hargreaves equation based on mean annual temperatures. Though there are other methods to calculate PET, such as the Penman–Monteith equation [50] and the Thornthwaite equation [51], the biggest advantage of the Hargreaves equation is that it is more applicable to estimate PET for long time steps [52].

Additional data, such as the updated high-resolution vegetation types (1:1,000,000) [53] were collected from the website (<https://gfbica06e19c435df441bhq6vwbbwpuknx6bvnfiac.eds.tju.edu.cn/#/>, accessed on 5 September 2022). The delineation of karst and non-karst regions was based on the results of China geological surveys. The administrative boundaries were sourced from the Resource and Environment Science and Data Center, Chinese Academy of Sciences (<https://www.resdc.cn/>, accessed on 17 September 2022). In order to conduct the analysis, we re-sampled all the grid data at 5 km × 5 km with the timescale from 1990 to 2018.

2.3. Methodology

2.3.1. Reconstructing NDVI Time-Series Based on EEMD

The flowchart of the methodology is shown in Figure 3. First, EEMD is a newly developed adaptive method for signal analysis of nonlinear and non-stationary time-series data and has been improved based on the empirical mode decomposition (EMD) method [54]. EEMD decomposes the raw NDVI time series into several intrinsic mode functions (IMFs) components with different period scales and a trend component by adding white noise to the raw data and then calculating the ensemble average, which effectively alleviates the “mode mixing” problem of EMD and retains binary filter capability [24]. The decomposition process can be described as Equation (1), but it is worth noting that all IMFs must meet two conditions, namely (1) the numbers of extreme points and zero points must be equal to or differ by at most one; and (2) the mean value of the up-and-down envelope corresponding to the maxima and minima is zero at any time [25].

$$S(t) = \sum_{i=1}^n IMF(t) + R(t) \tag{1}$$

In this study, all pixel values of monthly NDVI data from 1990 to 2018 were spatially averaged, and an original $S(t)$ time series with 348 values was obtained. Noises were iteratively added with 100 numbers and a 0.1 standard deviation to the standardized series, then we obtained IMFs and residual $R(t)$; the results are shown in Figure 4. All processing was implemented in MATLAB2021b; the EEMD package was sourced from National Central University (<https://ncu.edu.tw/>, accessed on 23 June 2022).

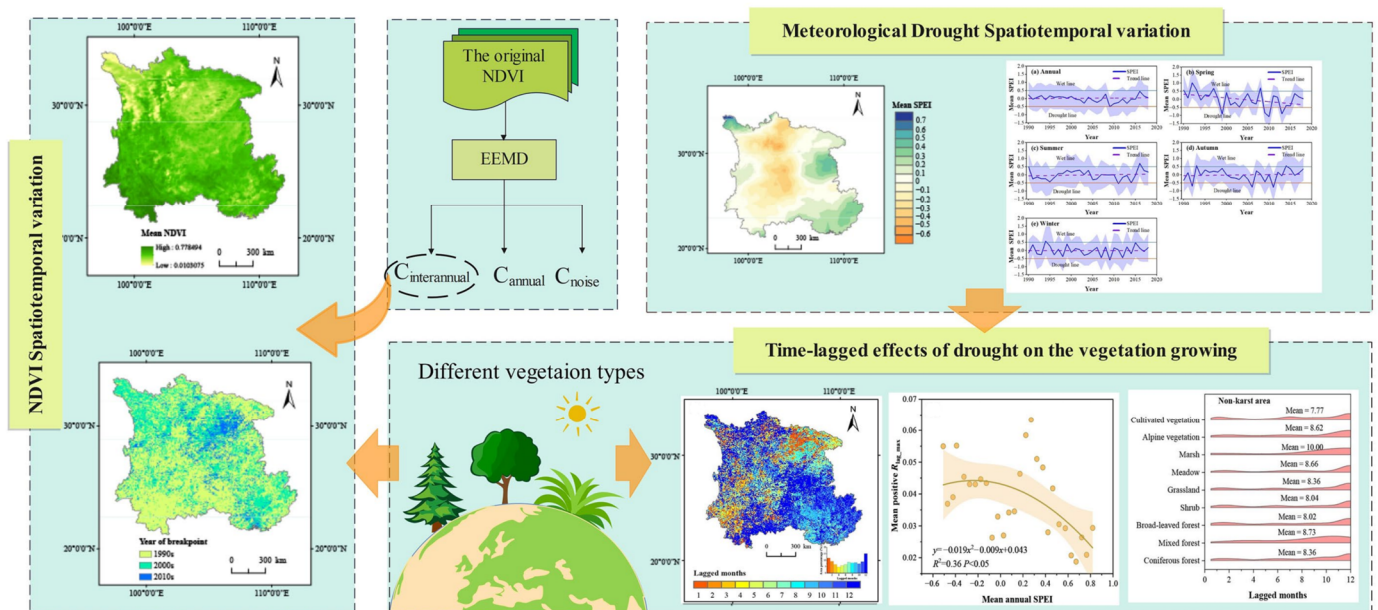


Figure 3. Overall framework for this study.

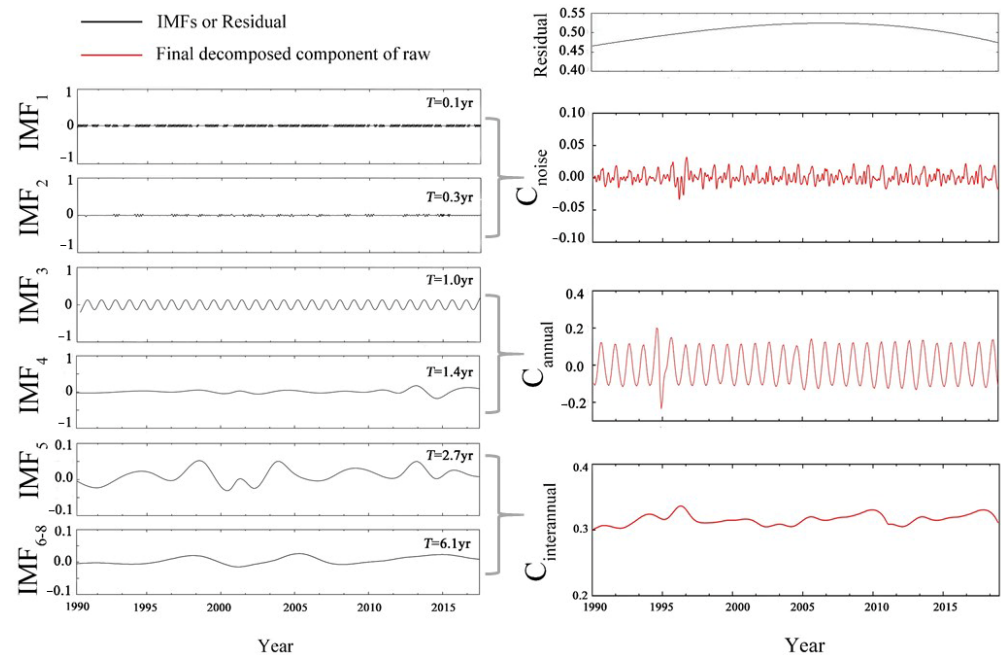


Figure 4. The architecture of EEMD for reconstructing NDVI time series.

2.3.2. Analyzing Linear and Nonlinear Trends in Interannual NDVI

In this study, an ordinary least squares linear regression method was taken to detect the overall trends of the NDVI interannual component from 1990 to 2018:

$$y_i = a_0 + b_0x + \varepsilon \quad (2)$$

where y_i indicates the dependent variable interannual NDVI and x is the time; a_0 and b_0 represent regression intercept and slope, respectively; ε is the error term.

The interannual variation of NDVI was probably disturbed by sudden events, such as wildfires, droughts and insect attacks, but such abrupt changes can be overshadowed in the overall trend [55]. Therefore, we used the BFAST detection method to detect abrupt changes in vegetation growth, and the trends in the NDVI time series differed before and after the breakpoint. The main detection processes for breakpoints in time and space sequences were implemented in R. When setting the seasonal model for the input parameters, the seasonal element of the NDVI time series was removed in the EEMD process, so we set the seasonal model to “none”. To avoid overly complex results and detect the most significant breakpoint, we also set the maximum number of breakpoints to 1.

2.3.3. Calculating Standardized Precipitation and Evapotranspiration Index (SPEI)

SPEI is a widely used meteorological index in drought research proposed by Vicente Serrano et al. [56]. Based on climatic water balance, it is calculated by integrating meteorological elements such as temperature, precipitation and evapotranspiration. We used the monthly mean precipitation and PET to calculate the monthly SPEI across southwest China from 1990 to 2018; the main procedures are as follows:

Step 1: The accumulation series of moisture gain and loss on different time scales D_i was established.

$$D_i = P_i - PET_i \quad (3)$$

PET_i and P_i indicate monthly potential evapotranspiration and precipitation, respectively, and D_i represents the differential between precipitation and evapotranspiration.

Step 2: Since there may be negative values in the original data sequence D_i , the 3-parameter Log-logistic probability distribution was used to standardize the cumulative probability density; the general form of the probability density function is as follows.

$$F(x) = \left[1 + \left(\frac{\alpha}{x - \gamma} \right)^\beta \right]^{-1} \quad (4)$$

Here is how to calculate α, β, γ :

$$\begin{cases} \alpha = \frac{(\omega_0 - 2\omega_1)\beta}{\Gamma(1+1/\beta)\Gamma(1-1/\beta)} \\ \beta = \frac{2\omega_1 - \omega_0}{6\omega_1 - \omega_0 - 6\omega_2} \\ \gamma = \omega_0 - \alpha\Gamma(1+1/\beta)\Gamma(1-1/\beta) \end{cases} \quad (5)$$

Γ is the factorial function; $\omega_0, \omega_1, \omega_2$ are the probability-weighted moments of the data sequence D_i .

Step 3: To calculate *SPEI*, convert the cumulative probability to a normal standard variable with mean zero and variance 1.

$$P = 1 - F(x) \quad (6)$$

When $p \leq 0.5$,

$$\omega = \sqrt{-2 \ln(P)} \quad (7)$$

$$SPEI = \omega - \frac{C_0 + C_1\omega + C_2\omega^2}{1 + d_1\omega + d_2\omega^2 + d_3\omega^3} \quad (8)$$

In the formula, $C_0 = 2.515517$, $C_1 = 0.802853$, $C_2 = 0.010328$, $d_1 = 1.432788$, $d_2 = 0.189269$, $d_3 = 0.001308$. If the p -value is larger than 0.5, then the value of p is replaced with $p-1$.

To analyze seasonal droughts in southwest China, we calculated cumulative *SPEI* values on a three-month time scale in May, August, November and the following February as *SPEI* of spring, summer, autumn, and winter, respectively. The *SPEI* algorithm was implemented by the “*SPEI*” package in Python (<http://hdl.handle.net/10261/10002>, accessed on 14 May 2022). The drought classification criteria are presented in Table 1.

Table 1. Drought classification criteria based on *SPEI*.

SPEI Values	Class
$0.5 \leq \text{SPEI}$	No drought
$-0.5 \leq \text{SPEI} < 0.5$	Semi-arid or semi humid
$-1.0 \leq \text{SPEI} < -0.5$	Mild drought
$-1.5 \leq \text{SPEI} < -1.0$	Moderate drought
$\text{SPEI} \leq -1.5$	Severe drought

2.3.4. Determining the Time-Lagged Effect of Drought on Vegetation

To assess the time-lagged effect of drought on vegetation growth, the Pearson correlation coefficient (r) was used. We aimed to determine the maximum significant correlation coefficient (R_{\max_lag}) between the present NDVI and the 1-month *SPEI* of the previous 12 months and in which month it occurred. Specifically, we combined the NDVI of each month with the 1-month *SPEI* of the previous i months to create a time series, and computed r with a time scale of i months (Equation (9)). Then, the R_{\max_lag} was determined when r_i was the maximum correlation coefficient of each grid; the corresponding i was the time scale of the lag month (Equation (10)). For example, if the R_{\max_lag} occurred between

the monthly NDVI in April and the 1-month SPEI in November of the previous year, the time-lagged scale was 5 months.

$$r_i = \text{corr}(\text{NDVI}, \text{SPEI}_i) \quad 0 \leq i \leq 12 \quad (9)$$

$$R_{\text{max_lag}} = \max(r_i) \quad 0 \leq i \leq 12 \quad (10)$$

where: i represents the lag month (0 indicated no lagged effect), r_i is the Pearson correlation coefficient, NDVI is the monthly NDVI time series based on EEMD, and SPEI_i means the monthly SPEI time series with a lag of i months.

In addition, to further estimate the relationship between water balance and time-lagged scales, we used the cumulative SPEI in December (i.e., annual SPEI) covering 1990–2018, which represented the annual water balance conditions. The water balance gradient was identified by the equal interval of the mean value of the annual SPEI (0.1) [34,57].

3. Results

3.1. Spatiotemporal Variations and Abrupt Change in Vegetation Growth

The interannual NDVI in southwest China displayed significant spatial heterogeneity. The mean values ranged from 0.01 to 0.78 from 1990 to 2018 and were higher in the southwest of the study area than that in the northeast (Figure 5a). By comparing the mean NDVI of different vegetation types between non-karst and karst areas, it was found that, except for marsh and alpine vegetation, the vegetation in non-karst areas grew better than in karst areas (Figure 5b).

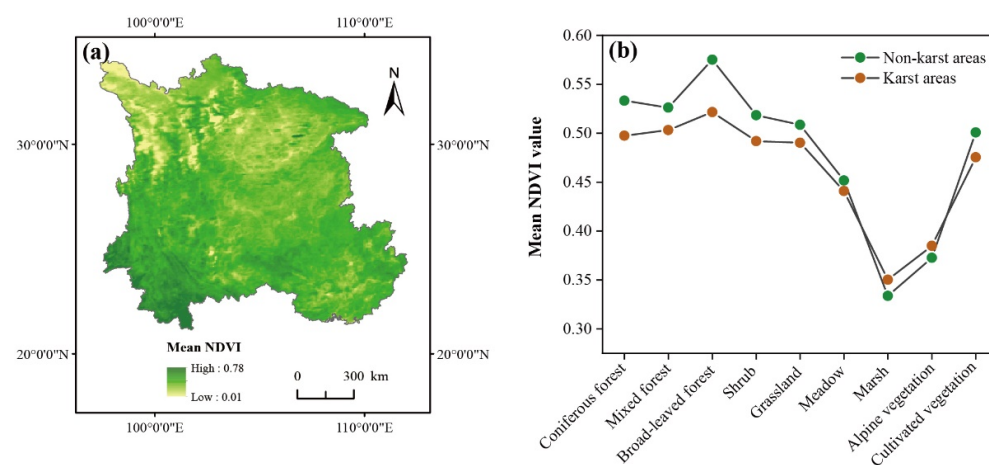


Figure 5. (a) Spatial distribution of interannual mean NDVI after reconstructing from 1990 to 2018; (b) interannual mean NDVI value of different vegetation types in karst and non-karst areas from 1990 to 2018.

In general, for the past 30 years, the vegetation growth in both non-karst and karst areas has shown a significant greening trend, with the interannual NDVI increasing at a rate of 0.0396/10a and 0.0357/10a, respectively (Figure 6a). Based on the linear analysis, approximately 97% of the whole study area was observed to have a distinctly greening trend (slope > 0, $p < 0.05$) during the period of 1990–2018 (Figure 6b). The greening trend of different vegetation types varied slightly (Figure 6c); the interannual NDVI increasing trends of coniferous forest, grassland and cultivated vegetation were higher than others, and the vegetation greening trend was stronger in karst areas than in non-karst areas, except marsh.

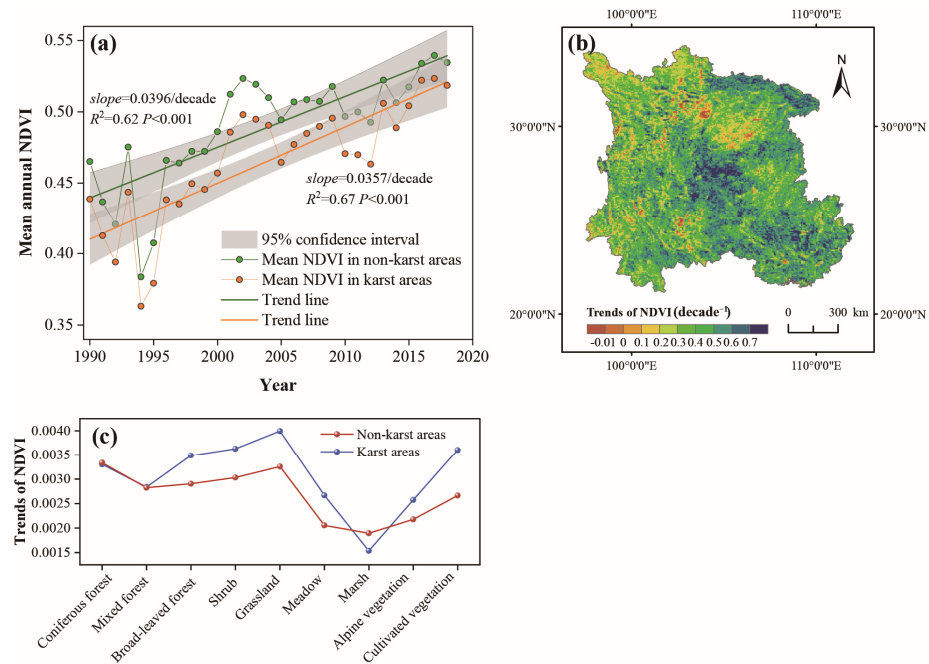


Figure 6. (a) Temporal change trends in interannual mean NDVI from 1990 to 2018. (b) Spatial change trends in interannual mean NDVI from 1990 to 2018. (c) The mean change trends of different vegetation types in karst and non-karst areas from 1990 to 2018.

For southwest China, we detected an interannual NDVI trend breakpoint by BFAST in 1995 (Figure 7). Before the breakpoint, the vegetation greening trend was not significant ($slope = 0.0005 \text{ year}^{-1}$, $p = 0.82$); after the breakpoint, this trend showed a clear and sharp increase ($slope = 0.0033 \text{ year}^{-1}$, $p < 0.001$). Furthermore, we detected breakpoints across different vegetation types (Figure 8). The breakpoints of coniferous forest, mixed forest, broad-leaved forest, shrub, grassland, marsh, and cultivated vegetation all occurred near 1995, while meadow and alpine vegetation were found around 2000. Before the breakpoint, unlike the decreasing trend shown by coniferous forests, mixed forest, and marsh ($slope = -0.0114$ – $-0.0021 \text{ year}^{-1}$), the interannual NDVI of other vegetation types exhibited a weakly significant increase ($slope = 0.0003$ – 0.0042 year^{-1}); after the breakpoint, the NDVI variations of other vegetation types increased rapidly ($slope = 0.0005$ – 0.0043 year^{-1}), except for alpine vegetation and meadow.

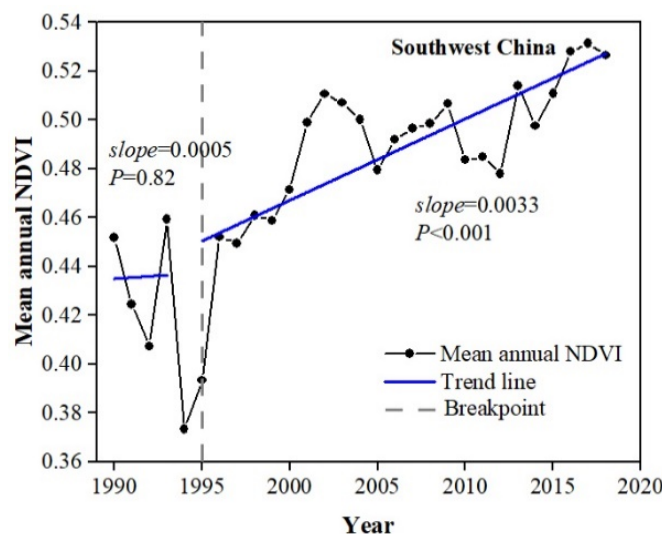


Figure 7. Abrupt change in trends based on BFAST algorithm in NDVI from 1990 to 2018.

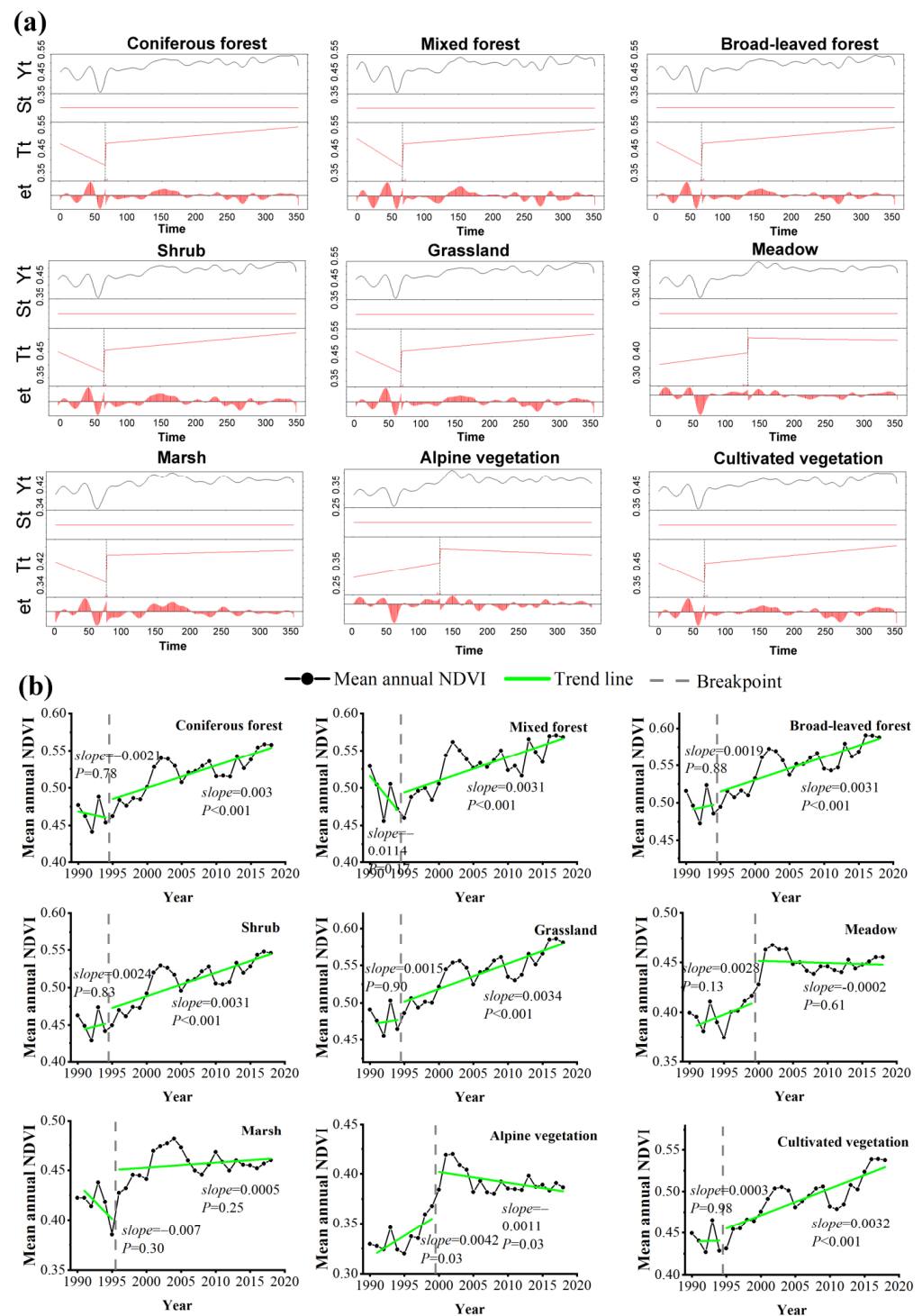


Figure 8. BFAST results for mean NDVI in the different vegetation types of southwest China. (a) Abrupt breakpoints detected. Yt: the observed data at time t, St: the period component, Tt: the long-term trend component, et: the remaining component, t: the time of the observation; the X-axis is spaced in months, e.g., 1 for January 1990 and 348 for December 2018. (b) Abrupt change in trends.

Spatially, almost all grids of southwest China had breakpoints in interannual NDVI trends, more than half of which occurred in the 1990s (with a proportion of 59.43%), mainly distributed in the southwest of the study area (Figure 9a). Only approximately 10% of the breakpoint pixels occurred in the 2010s, mainly located in the Sichuan Basin. By analyzing the years when the breakpoints appeared in the karst and non-karst areas, it was found that a majority of breakpoints in both areas mainly appeared during 1995–2000; before

1995, there was little breakpoint (Figure 9b). For the karst areas, the proportion of pixels with breakpoints in the 1990s, 2000s, and 2010s were 58.1%, 30.6%, and 11.3% of the region, respectively, but for non-karst areas were 61.5%, 29%, and 9.5%, respectively.

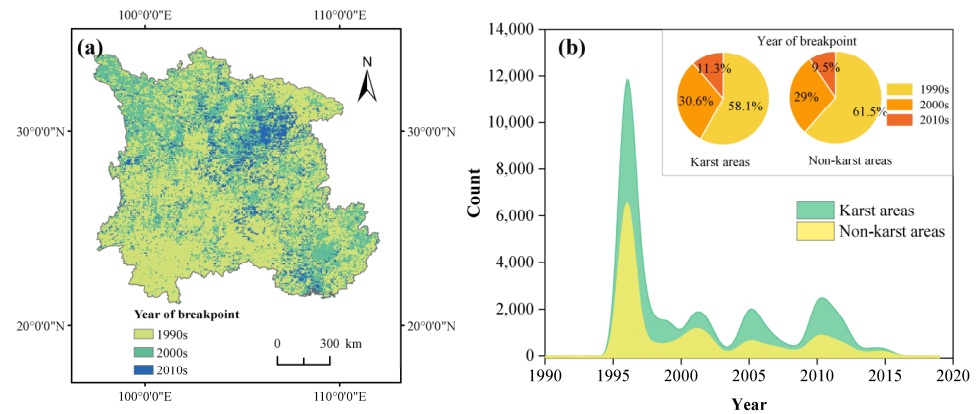


Figure 9. (a) Spatial distribution of the timing of breakpoints. (b) Timing of breakpoints in karst and non-karst areas.

3.2. Meteorological Drought Spatiotemporal Changes

The spatial patterns of the mean SPEI for the whole year and for spring, summer, autumn, and winter from 1990 to 2018 are represented in Figures 10 and 11a–d. The mean SPEI values for the whole year were lower in the middle and higher ground, and only 0.9% of the study area was under mild drought. Meanwhile, there was a significant difference in the water balance conditions for the four seasons. The order of the mean SPEI was summer (0.25) > winter (−0.11) > spring (−0.53) > autumn (−0.91). In spring, nearly 46.53% of the study area suffered from mild drought and 13.84% was under moderate drought; in summer, only 9.7% of the pixels experienced mild drought, mainly in the north region. In autumn, over half of the area was subjected to moderate drought (approximately 53.97%), and this was mainly concentrated in the south and northwest of the study area. In winter, 21.24% and 19.39% of the pixels experienced mild and moderate drought, respectively.

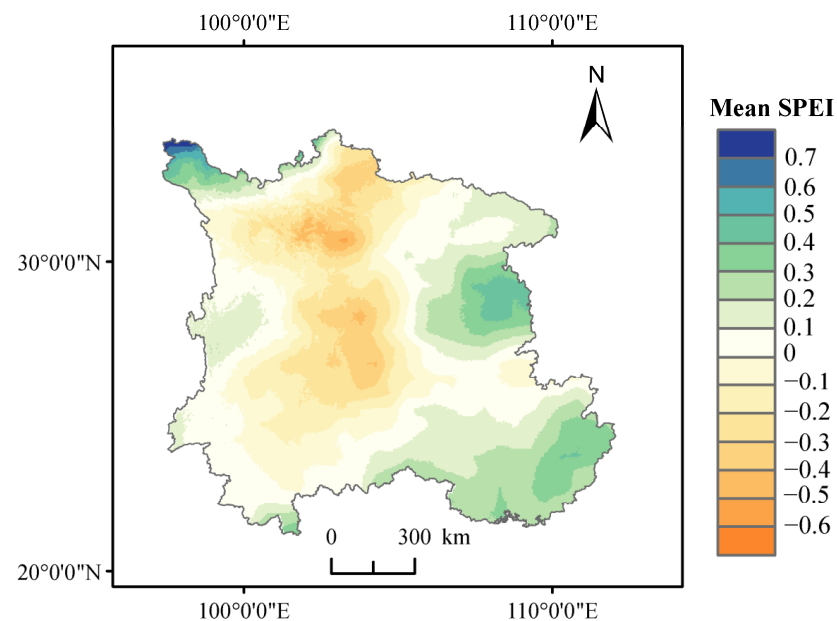


Figure 10. Spatial distribution of annual mean SPEI from 1990 to 2018.

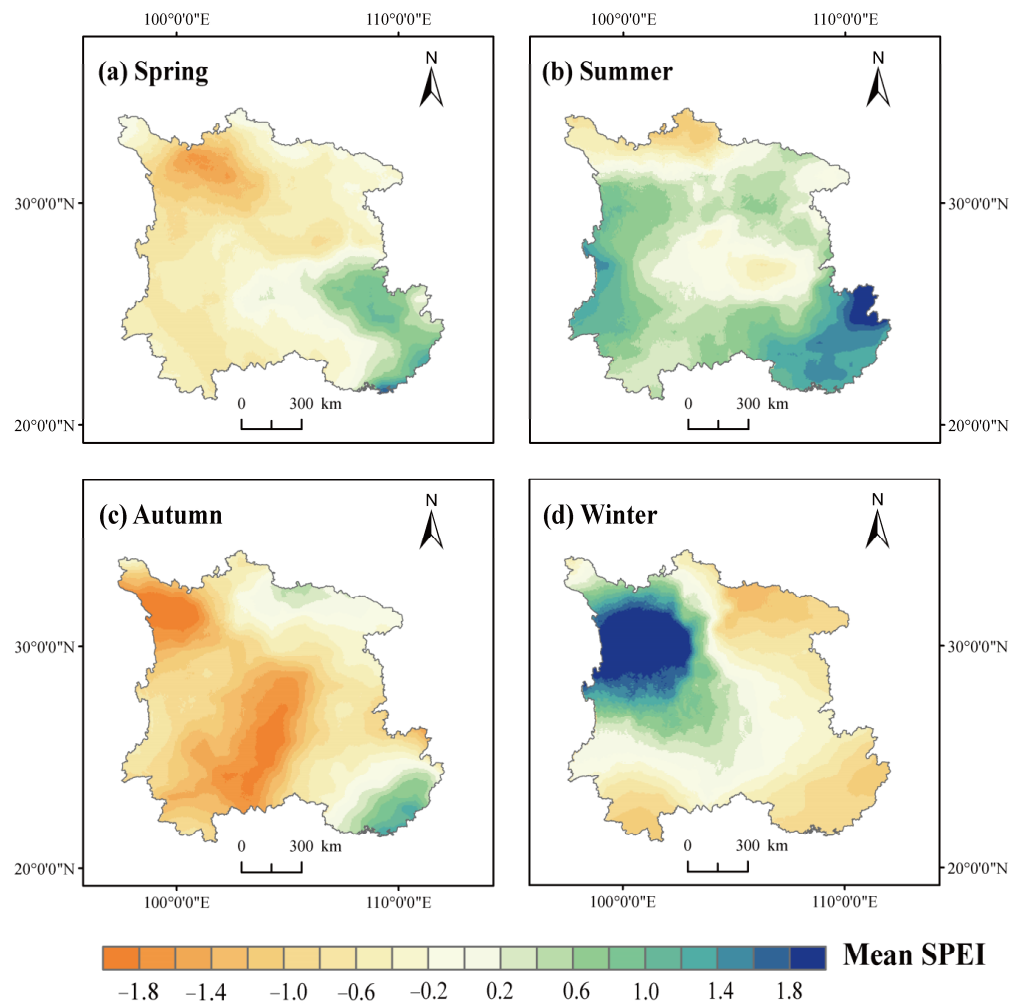


Figure 11. Spatial distribution of mean SPEI from 1990 to 2018. (a) Spring; (b) summer; (c) autumn; (d) winter.

Figure 12 illustrates the change trends of SPEI in the whole year and the four seasons of southwest China from 1990 to 2018. In general, SPEI showed an upward trend at a rate of 0.0014 year^{-1} . The year 2009 was the driest year in southwest China with an SPEI value of -0.48 , while 2016 was the wettest year with an SPEI of 0.45 . In addition, it was found that the trend of drought alleviation appeared in all seasons except for spring. In summer, autumn, and winter, the SPEI increased at rates of 0.0033 year^{-1} , 0.0031 year^{-1} , and 0.0001 year^{-1} , respectively. In contrast, the SPEI in spring showed a decreasing trend at the rate of -0.023 , indicating a marked trend towards drought.

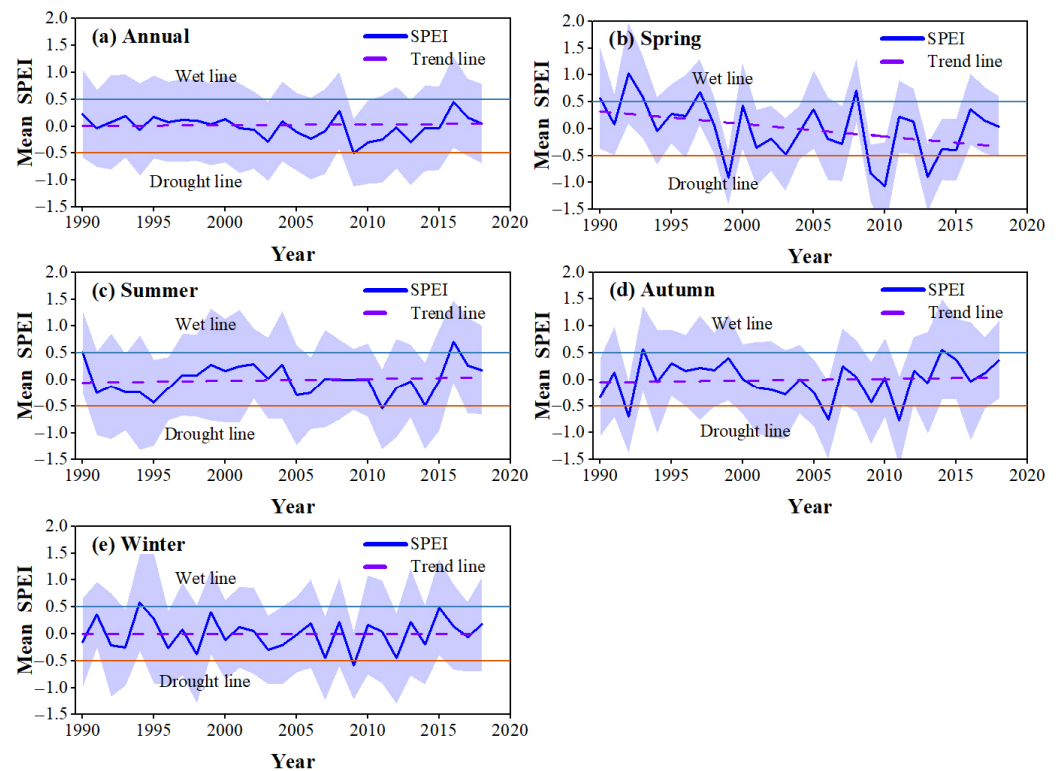


Figure 12. Temporal change trends in mean SPEI from 1990 to 2018. (a) Annual; (b) spring; (c) summer; (d) autumn; (e) winter.

Figure 13a represents spatial pattern of trends in annual SPEI across southwest China. The change trends ranged from -0.039 year^{-1} to 0.034 year^{-1} for the period between 1990 and 2018. We observed a significant decrease in SPEI across the west of the study area ($p < 0.05$), accounting for 34.64% of the total area. For seasons, the spatial patterns in SPEI change trends differed. As shown in Figure 13b–e, the drought trend increased most strongly in spring (nearly 94.27% of the pixels), followed by winter, and was alleviated in autumn and summer. In spring, the drought intensified as a whole except for in the Sichuan Basin and the southern Yunnan Province. In summer, 36.07% of areas had a decrease in SPEI, and the drought was alleviated in the center of the study area. In autumn and winter, drought reduction was concentrated in the eastern regions.

3.3. Time-Lagged Effect of Drought on Vegetation

Figure 14a shows the spatial pattern of the maximum correlation coefficient ($R_{\text{max_lag}}$) between NDVI and SPEI. In general, 87.63% of the vegetation had a significant correlation, with 67.94% and 19.67% of the grids having positive and negative correlations, respectively. The highest positive $R_{\text{max_lag}}$ was more than 0.24, primarily observed in the Sichuan Basin. Negative correlations were mainly found northwest of the study area.

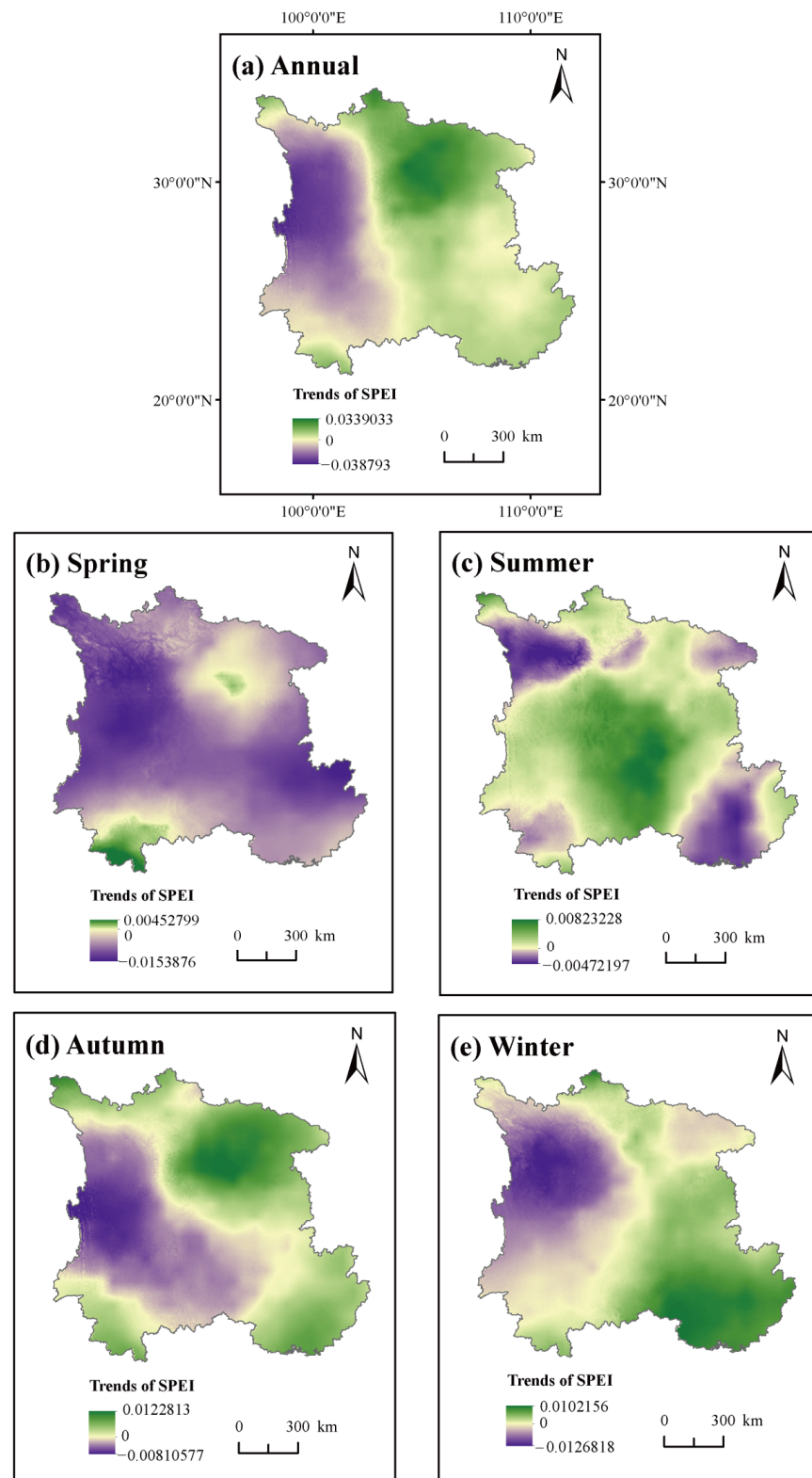


Figure 13. Spatial change trends in mean SPEI from 1990 to 2018. (a) Annual; (b) spring; (c) summer; (d) autumn; (e) winter.

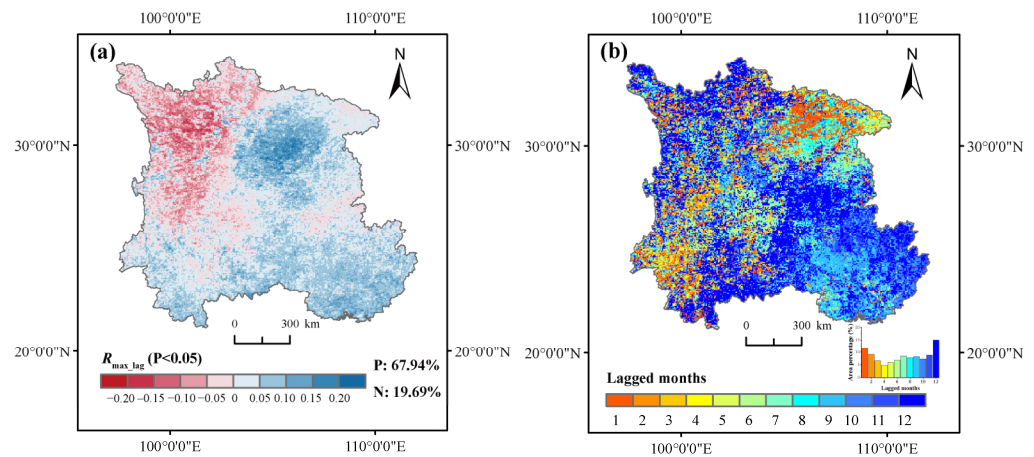


Figure 14. (a) Spatial distribution of the R_{\max_lag} between SPEI and NDVI from 1990 to 2018. (b) Spatial distribution of time-lagged months when R_{\max_lag} occurred.

For the pixels with time-lagged effect (Figure 14b), the lag time was observed from 1 to 12 months. The percentage with a lag time of 12 months was the highest, accounting for 15.03% of the vegetation lands, followed by a 1-month lag (11.63%), and the smallest area percentage was found in the 4-month lag, only accounting for 4.71%. Moreover, nearly 27.28% of the vegetation lands had a short time lag (i.e., 1 to 3 months), mostly in the northeast and southwest of the study area. For the long time scales (i.e., 9 to 12 months), these were mainly located in the southeast with a percentage area of 39.28%.

Overall, the mean lag months were shorter in karst than in non-karst areas, indicating that vegetation in this area was more frequently affected by drought. In non-karst areas, approximately 55.17% of the grids had a lag time greater than 9 months, compared to 42.40% in karst areas (Figure 15a). For the different vegetation types, regardless of karst or non-karst areas, the marsh exhibited the longest lagged months while cultivated vegetation was the shortest (Figure 15b,c). The grassland, shrub, and broad-leaved forest in karst areas showed longer response time to drought than those in non-karst areas, but for the other vegetation types, the mean lagged time was not clearly different.

Through statistical analysis, potential relationships were found between the water balance gradient (mean SPEI) and R_{\max_lag} and the lag time scales (Figure 16). As the mean annual SPEI increased, the mean value of the positive R_{\max_lag} increased at first and then dropped ($R^2 = 0.36$, $p < 0.05$), which means that the intensity of the time-lagged effect of drought on vegetation growth weakened as water conditions improved (Figure 16a). There was a U-shaped relationship between the lagged time scale and mean SPEI, indicating that in areas with more favorable hydrological conditions, the drought effects on vegetation would be apparent only after a longer period of time (Figure 16b).

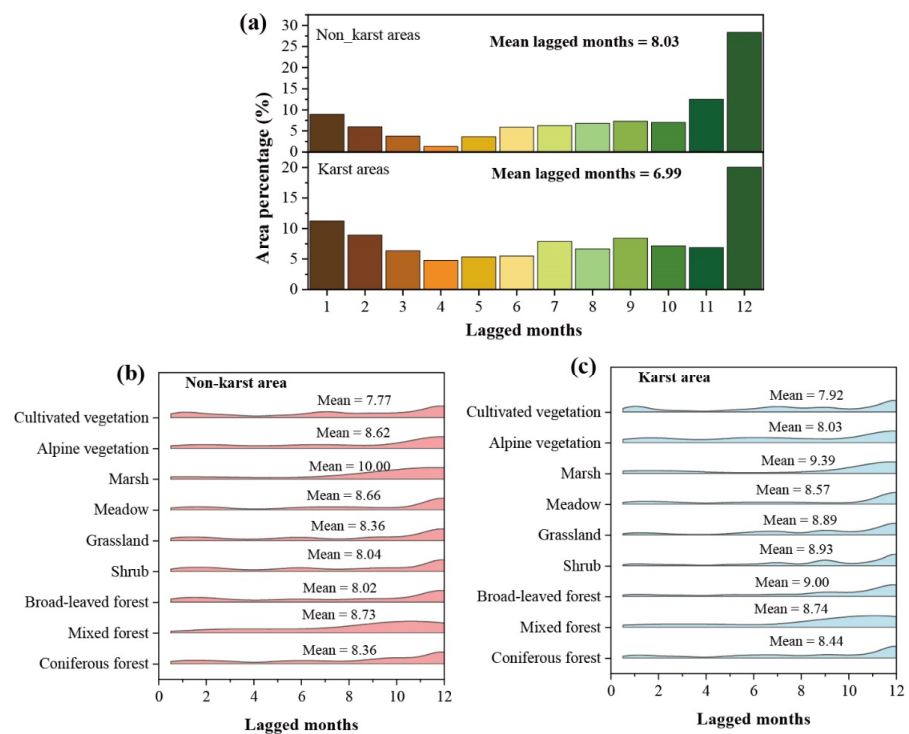


Figure 15. (a) Area percentage at different lagged time scales in karst and non-karst areas. (b) Time-lagged months of different vegetation types in karst areas. (c) Time-lagged months of different vegetation types in non-karst areas.

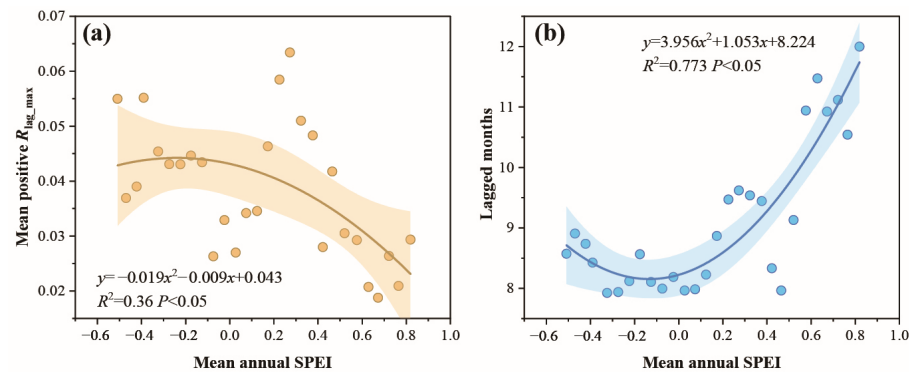


Figure 16. (a) Relationships between mean annual SPEI and positive R_{max_lag} . (b) Relationships between mean annual SPEI and lagged months.

4. Discussion

As a major carbon reservoir in China, as well as a typical ecologically fragile area, the vegetation restoration in southwest China has been of great concern. This study reconstructed NDVI using EEMD for long-term trend study and found that 95% of the vegetation in southwest China showed a greening trend and a significant increase in vegetation cover over the past three decades, further indicating that southwest China has become a hotspot for vegetation growth [58,59]. In contrast, the greening rate of karst areas (0.0357/10a) was slower than that of non-karst areas (0.0396/10a), which may be related to the special topographical features of karst areas. The high permeability of limestone makes the surface water in karst areas extremely susceptible to loss with poor soil development conditions [60], which is not conducive to the growth and development of vegetation. However, the increasing trend of interannual NDVI was not continuous, and we found that 59.43% of the study area experienced a trend reversal in the 1990s using BFAST breakpoint detection. Vegetation in most areas showed a rapid upward trend after the breakpoint,

but alpine vegetation tended to decline. This abrupt change in the vegetation greening process is often ignored; in fact, the analysis of the abrupt change and understanding of the hidden changes in the greening would help to reveal the actual trend of vegetation growth and grasp the potential risk of vegetation browning [1,23,61]. Ecological restoration projects are considered to be the main driver for accelerated vegetation greening after abrupt change [62]. Since 2000, a series of forestry conservation management projects have been implemented in southwest China to combat the increasing stone desertification in karst areas, including the Grain to Green Program and natural forest protection, which have enabled a great improvement in vegetation cover, supported by the study of Tong et al. [36].

Previous studies have used different drought indices to quantify the meteorological drought variability and the severity of drought events in southwest China [63,64]. In this study, we found that drought intensity was enhanced in the western part of the study area by calculating the SPEI trends, which was consistent with the findings of Sun et al. [65]. In the context of climate warming, the weakened Indian Ocean monsoon has reduced water vapor availability, which has led to more severe drought trends in this region [66,67]. Meanwhile, spring drought has significantly intensified, and the water deficit before the vegetation green-up period will have a serious negative impact on the vegetation growth in the middle and late growing seasons, which may lead to increased ecosystem vulnerability to drought [68,69].

Understanding the drought–vegetation relationship is essential for predicting vegetation growth and ecosystem productivity under global warming. However, this will remain a challenge in the future, as previous studies have demonstrated that early moisture conditions could affect current vegetation growth [33], and the findings in this study also found that vegetation growth tends to respond with a lag to drought events. However, for different regions, there are obvious differences in the time-lagged months. It was found that the lag time in karst areas was one month shorter than that in non-karst areas, mainly because the rocks in karst areas have larger pores and fissures with strong infiltration, and also the shallower soil layer is not conducive to water storage, which makes the response time of vegetation to drought shorter in this region [70]. For the different vegetation types, the marsh and mixed-forest exhibit longer lagged months, which may be attributed to the fact that different vegetation types have different responses and adaptation strategies to drought [71]. Woody plants, characterized by species richness and complex root systems [72], can self-regulate to adapt to various climatic and hydrological conditions [73]. These results will improve our understanding of the drought–vegetation relationships. When assessing ecological health in the future, more attention should be paid to the time-lagged effect of drought on different vegetation types and to developing appropriate ecological restoration management measures based on the natural conditions in karst and non-karst areas to achieve improved overall drought resistance of vegetation for future climate change.

The AVHRR NDVI dataset has good performance in monitoring long-term vegetation cover, but there are still some limitations. In this study, NDVI data at 5km resolution were used to analyze different vegetation types, neglecting the more fine-scale vegetation fragmentations. Furthermore, fragmented vegetation types have strong scale differences [74] and a single scale analysis is not conducive to capturing the real condition of vegetation NDVI.

5. Conclusions

In this study, we monitored the overall NDVI evolution trends and abrupt changes after Ensemble Empirical Mode Decomposition (EEMD) reconstruction in southwest China from 1990 to 2018. Subsequently, we analyzed the seasonal drought evolution trends using the standardized precipitation and evapotranspiration index (SPEI), as well as the lag effect of drought on vegetation growth across karst and non-karst areas. The results showed that 97% of the whole study area observed a gradually greening trend from 1990 to 2018. However, this greening trend has a non-linear characteristic, and we found an abrupt

change in 1995 over the whole study area using the Breaks for Additive Seasonal and Trend (BFAST) algorithm, where the vegetation greening trend increased rapidly after the mutation point. For most of the vegetation types, the breakpoint occurred in the 1990s, and the breakpoint occurrence time and the trend before and after the breakpoint differed across vegetation types. Moreover, the drought in the study area gradually intensified during the study period, especially in the western region. In regard to seasonality, drought in spring and winter significantly intensified, while it eased in summer and autumn. The shortage of water in the previous period can affect current vegetation growth, and the time-lagged months in this area ranged from 1–12. Nearly 27.28% of the vegetation lands had a lag time of less than 3 months, mostly in the northeast and southwest of the study area. A U-shaped relationship was observed between SPEI and lag months, i.e., the better the moisture conditions, the longer the lag time. The mean lagged time scales in karst areas were shorter than in non-karst areas, the vegetation in this area was much less drought tolerant. For various vegetation types, the mixed forest and marsh had a longer lagged time and were more resistant to drought than other vegetation types. Our study reveals the non-linear characteristics of different vegetation types in karst and non-karst areas and the lagged response to drought, which is helpful for gaining a deeper understanding of the evolutionary trends of vegetation and a more accurate grasp of the relationship between vegetation and drought.

Author Contributions: Conceptualization, P.J.; Methodology, Y.H.; Software, Y.W. and X.G.; Formal analysis, Y.W. and Y.Y.; Resources, P.J.; Data curation, Y.Y. and X.G.; Writing—original draft, Y.W.; Writing—review & editing, P.J., L.L. (Lei Liu) and L.L. (Liang Liu); Supervision, Y.H.; Funding acquisition, L.L. (Liang Liu). All authors have read and agreed to the published version of the manuscript.

Funding: This study was funded by the Sichuan Soft Science Research Program Projects (project numbers: 2023JDR0278 and 2022JDR0177), the National Natural Science Foundation of China (project numbers: 72004188) and the Sci-tech Plan Projects of Tibet Autonomous Region (project numbers: XZ202201ZY0015).

Institutional Review Board Statement: Not applicable.

Informed Consent Statement: Not applicable.

Data Availability Statement: The data presented in this study are available on request from the corresponding author.

Acknowledgments: We thank the National Tibetan Plateau Data Centre and the National Earth System Science Data Center of China for NDVI and meteorological data.

Conflicts of Interest: The authors declare no conflict of interest.

References

1. Wen, Z.F.; Wu, S.J.; Chen, J.L.; Lu, M.Q. NDVI indicated long-term interannual changes in vegetation activities and their responses to climatic and anthropogenic factors in the Three Gorges Reservoir Region, China. *Sci. Total Environ.* **2017**, *574*, 947–959. [[CrossRef](#)]
2. Komatsu, K.J.; Avolio, M.L.; Lemoine, N.P.; Isbell, F.; Isbell, F.; Grman, E.; Houseman, G.R.; Koerner, S.E.; Johnson, D.S.; Wilcox, K.R.; et al. Global change effects on plant communities are magnified by time and the number of global change factors imposed. *Proc. Natl. Acad. Sci. USA* **2019**, *116*, 17867–17873. [[CrossRef](#)]
3. Shi, Y.; Jin, N.; Ma, X.L.; Wu, B.Y.; He, Q.S.; Yue, C.; Yu, Q. Attribution of climate and human activities to vegetation change in China using machine learning techniques. *Agric. For. Meteorol.* **2020**, *294*, 108146. [[CrossRef](#)]
4. Xu, L.; Samanta, A.; Costa, M.H.; Ganguly, S.; Nemani, R.R.; Myneni, R.B. Widespread decline in greenness of Amazonian vegetation due to the 2010 drought. *Geophys. Res. Lett.* **2011**, *38*, L07402. [[CrossRef](#)]
5. De Jong, R.; Verbesselt, J.; Schaepman, M.E.; De Bruin, S. Trend changes in global greening and browning: Contribution of short-term trends to longer-term change. *Global Chang. Biol.* **2012**, *18*, 642–655. [[CrossRef](#)]
6. Nouri, H.; Anderson, S.J.; Sutton, P.C.; Beecham, S.; Nagler, P.L.; Jarchow, C.J.; Roberts, D.A. NDVI, scale invariance and the modifiable areal unit problem: An assessment of vegetation in the Adelaide Parklands. *Sci. Total Environ.* **2017**, *584*, 11–18. [[CrossRef](#)] [[PubMed](#)]

7. Yang, L.Q.; Guan, Q.Y.; Lin, J.K.; Tian, J.; Tan, Z.; Li, H.C. Evolution of NDVI secular trends and responses to climate change: A perspective from nonlinearity and nonstationarity characteristics. *Remote Sens. Environ.* **2021**, *254*, 112247. [[CrossRef](#)]
8. Zhang, Y.; Gentine, P.; Luo, X.Z.; Lian, X.; Liu, Y.L.; Zhou, S.; Michalak, A.M.; Sun, W.; Fisher, J.B.; Piao, S.L.; et al. Increasing sensitivity of dryland vegetation greenness to precipitation due to rising atmospheric CO₂. *Nat. Commun.* **2022**, *13*, 4875. [[CrossRef](#)]
9. Sha, Z.Y.; Bai, Y.F.; Li, R.R.; Lan, H.; Zhang, X.L.; Li, J.T.; Liu, X.F.; Chang, S.J.; Xie, Y.C. The global carbon sink potential of terrestrial vegetation can be increased substantially by optimal land management. *Commun. Earth Environ.* **2022**, *3*, 8. [[CrossRef](#)]
10. Chen, C.; Park, T.; Wang, X.H.; Piao, S.L.; Xu, B.D.; Chaturvedi, R.K.; Fuchs, R.; Brovkin, V.; Ciais, P.; Fensholt, R. China and India lead in greening of the world through land-use management. *Nat. Sustain.* **2019**, *2*, 122–129. [[CrossRef](#)]
11. Xue, S.Y.; Xu, H.Y.; Mu, C.C.; Wu, T.H.; Li, W.P.; Zhang, W.X.; Streletskaya, I.; Grebenets, V.; Sokratov, S.; Kizyakov, A.; et al. Changes in different land cover areas and NDVI values in northern latitudes from 1982 to 2015. *Adv. Clim. Chang. Res.* **2021**, *12*, 456–465. [[CrossRef](#)]
12. Forzieri, G.; Dakos, V.; McDowell, N.G.; Ramdane, A.; Cescatti, A. Emerging signals of declining forest resilience under climate change. *Nature* **2022**, *608*, 534. [[CrossRef](#)] [[PubMed](#)]
13. Smith, T.; Traxl, D.; Boers, N. Empirical evidence for recent global shifts in vegetation resilience. *Nat. Clim. Chang.* **2022**, *12*, 477. [[CrossRef](#)]
14. Nunes, C.A.; Berenguer, E.; Frana, F.; Ferreira, J.; Lees, A.C.; Louzada, J.; Sayer, E.; Solar, R.; Smith, C.C.; Aragao, L.E.O.C.; et al. Linking land-use and land-cover transitions to their ecological impact in the Amazon. *Proc. Natl. Acad. Sci. USA* **2022**, *119*, e2202310119. [[CrossRef](#)] [[PubMed](#)]
15. Song, X.P.; Hansen, M.C.; Stehman, S.V.; Potapov, P.V.; Tyukavina, A.; Vermote, E.F.; Townshend, J.R. Global land change from 1982 to 2016. *Nature* **2018**, *563*, E26. [[CrossRef](#)]
16. Yang, Y.J.; Wang, S.J.; Bai, X.Y.; Tan, Q.; Li, Q.; Wu, L.H.; Tian, S.Q.; Hu, Z.Y.; Li, C.J.; Deng, Y.H. Factors Affecting Long-Term Trends in Global NDVI. *Forests* **2019**, *10*, 372. [[CrossRef](#)]
17. Pasquarella, V.J.; Arevalo, P.; Bratley, K.H.; Bullock, E.L.; Gorelick, N.; Yang, Z.Q.; Kennedy, R.E. Demystifying LandTrendr and CCDC temporal segmentation. *Int. J. Appl. Earth Obs.* **2022**, *110*, 102806. [[CrossRef](#)]
18. Diao, J.J.; Feng, T.; Li, M.S.; Zhu, Z.L.; Liu, J.X.; Biging, G.; Zheng, G.; Shen, W.J.; Wang, H.; Wang, J.R.; et al. Use of vegetation change tracker, spatial analysis, and random forest regression to assess the evolution of plantation stand age in Southeast China. *Ann. Forest Sci.* **2020**, *77*, 27. [[CrossRef](#)]
19. Browning, D.M.; Maynard, J.J.; Karl, J.W.; Peters, D.C. Breaks in MODIS time series portend vegetation change: Verification using long-term data in an arid grassland ecosystem. *Ecol. Appl.* **2017**, *27*, 1677–1693. [[CrossRef](#)]
20. Jamali, S.; Jonsson, P.; Eklundh, L.; Ardo, J.; Seaquist, J. Detecting changes in vegetation trends using time series segmentation. *Remote Sens. Environ.* **2015**, *156*, 182–195. [[CrossRef](#)]
21. Verbesselt, J.; Hyndman, R.; Zeileis, A.; Culvenor, D. Phenological change detection while accounting for abrupt and gradual trends in satellite image time series. *Remote Sens. Environ.* **2010**, *114*, 2970–2980. [[CrossRef](#)]
22. Ma, J.N.; Zhang, C.; Guo, H.; Chen, W.L.; Yun, W.J.; Gao, L.L.; Wang, H. Analyzing Ecological Vulnerability and Vegetation Phenology Response Using NDVI Time Series Data and the BFAST Algorithm. *Remote Sens.* **2020**, *12*, 3371. [[CrossRef](#)]
23. Pan, N.Q.; Feng, X.M.; Fu, B.J.; Wang, S.; Ji, F.; Pan, S.F. Increasing global vegetation browning hidden in overall vegetation greening: Insights from time-varying trends. *Remote Sens. Environ.* **2018**, *214*, 59–72. [[CrossRef](#)]
24. Hawinkel, P.; Swinnen, E.; Lhermitte, S.; Verbist, B.; Van Orshoven, J.; Muys, B. A time series processing tool to extract climate-driven interannual vegetation dynamics using Ensemble Empirical Mode Decomposition (EEMD). *Remote Sens. Environ.* **2015**, *169*, 375–389. [[CrossRef](#)]
25. Kong, Y.L.; Meng, Y.; Li, W.; Yue, A.Z.; Yuan, Y. Satellite Image Time Series Decomposition Based on EEMD. *Remote Sens.* **2015**, *7*, 15583–15604. [[CrossRef](#)]
26. Xue, P.; Liu, H.Y.; Zhang, M.Y.; Gong, H.B.; Cao, L. Nonlinear Characteristics of NPP Based on Ensemble Empirical Mode Decomposition from 1982 to 2015—A Case Study of Six Coastal Provinces in Southeast China. *Remote Sens.* **2022**, *14*, 15. [[CrossRef](#)]
27. McDowell, N.G.; Sapes, G.; Pivovarov, A.; Adams, H.D.; Allen, D.; Anderegg, W.R.L.; Arend, M.; Breshears, D.D.; Brodrigg, T.L.; Choat, B.; et al. Mechanisms of woody-plant mortality under rising drought, CO₂ and vapour pressure deficit. *Nat. Rev. Earth Environ.* **2022**, *3*, 294–308. [[CrossRef](#)]
28. Deng, Y.; Wang, X.H.; Wang, K.; Ciais, P.; Tang, S.C.; Jin, L.; Li, L.L.; Piao, S.L. Responses of vegetation greenness and carbon cycle to extreme droughts in China. *Agric. For. Meteorol.* **2021**, *298–299*, 108307. [[CrossRef](#)]
29. Zampieri, M.; Ceglar, A.; Dentener, F.; Toreti, A. Wheat yield loss attributable to heat waves, drought and water excess at the global, national and subnational scales. *Environ. Res. Lett.* **2017**, *12*, 64008. [[CrossRef](#)]
30. Rashid, I.; Majeed, U.; Najar, N.A.; Bhat, I.A. Retreat of Machoi glacier, Kashmir Himalaya between 1972 and 2019 using remote sensing methods and field observations. *Sci. Total Environ.* **2021**, *785*, 147376. [[CrossRef](#)]
31. Tang, W.X.; Liu, S.G.; Kang, P.; Peng, X.; Li, Y.Y.; Guo, R.; Jia, J.N.; Liu, M.C.; Zhu, L.J. Quantifying the lagged effects of climate factors on vegetation growth in 32 major cities of China. *Ecol. Indic.* **2021**, *132*, 108290. [[CrossRef](#)]
32. Wu, D.H.; Zhao, X.; Liang, S.L.; Zhou, T.; Huang, K.C.; Tang, B.J.; Zhao, W.Q. Time-lag effects of global vegetation responses to climate change. *Global Chang. Biol.* **2015**, *21*, 3520–3531. [[CrossRef](#)]

33. Wei, X.N.; He, W.; Zhou, Y.L.; Ju, W.M.; Xiao, J.F.; Li, X.; Liu, Y.B.; Xu, S.H.; Bi, W.J.; Zhang, X.Y.; et al. Global assessment of lagged and cumulative effects of drought on grassland gross primary production. *Ecol. Indic.* **2022**, *136*, 108646. [[CrossRef](#)]
34. Zhao, A.Z.; Yu, Q.Y.; Feng, L.L.; Zhang, A.B.; Pei, T. Evaluating the cumulative and time-lag effects of drought on grassland vegetation: A case study in the Chinese Loess Plateau. *J. Environ. Manag.* **2020**, *261*, 110214. [[CrossRef](#)]
35. Anderegg, W.R.L.; Schwalm, C.; Biondi, F.; Camarero, J.J.; Koch, G.; Litvak, M.; Ogle, K.; Shaw, J.F.; Shevliakova, E.; Williams, A.P.; et al. Pervasive Drought Legacy Effects in Forest Ecosystems and their Carbon Cycle Implications. *Science* **2015**, *349*, 528–532. [[CrossRef](#)] [[PubMed](#)]
36. Tong, X.W.; Brandt, M.; Yue, Y.M.; Horion, S.; Wang, K.L.; De Keersmaecker, K.; Tian, F.; Schurgers, G.; Xiao, X.M.; Luo, Y.Q.; et al. Increased vegetation growth and carbon stock in China karst via ecological engineering. *Nat. Sustain.* **2018**, *1*, 44–50. [[CrossRef](#)]
37. Zhang, X.M.; Brandt, M.; Yue, Y.M.; Tong, X.W.; Wang, K.L.; Fensholt, R. The Carbon Sink Potential of Southern China After Two Decades of Afforestation. *Earth's Future* **2022**, *10*, e2022EF002674. [[CrossRef](#)] [[PubMed](#)]
38. Liu, Y.Y.; Hu, Z.Z.; Wu, R.G.; Yuan, X. Causes and Predictability of the 2021 Spring Southwestern China Severe Drought. *Adv. Atmos. Sci.* **2022**, *39*, 1766–1776. [[CrossRef](#)]
39. Feng, Q.; Zhou, Z.F.; Zhu, C.L.; Luo, W.L.; Zhang, L. Quantifying the Ecological Effectiveness of Poverty Alleviation Relocation in Karst Areas. *Remote Sens.* **2022**, *14*, 5920. [[CrossRef](#)]
40. Peng, D.W.; Zhou, Q.W.; Tang, X.; Yan, W.H.; Chen, M. Changes in soil moisture caused solely by vegetation restoration in the karst region of southwest China. *J. Hydrol.* **2022**, *613*, 128460. [[CrossRef](#)]
41. Song, Z.H.; Xia, J.; She, D.X.; Li, L.C.; Hu, C.; Hong, S. Assessment of meteorological drought change in the 21st century based on CMIP6 multi-model ensemble projections over mainland China. *J. Hydrol.* **2021**, *601*, 126643. [[CrossRef](#)]
42. Cheng, Q.P.; Gao, L.; Zhong, F.L.; Zuo, X.A.; Ma, M.M. Spatiotemporal variations of drought in the Yunnan–Guizhou Plateau, southwest China, during 1960–2013 and their association with large-scale circulations and historical records. *Ecol. Indic.* **2020**, *112*, 106041. [[CrossRef](#)]
43. Wang, K.L.; Zhang, C.H.; Chen, H.S.; Yue, Y.M.; Zhang, W.; Zhang, M.Y.; Qi, X.K.; Fu, Z.Y. Karst landscapes of China: Patterns, ecosystem processes and services. *Landsc. Ecol.* **2019**, *34*, 2743–2763. [[CrossRef](#)]
44. NOAA CDR Program NOAA Climate Data Record (CDR) of AVHRR Normalized Difference Vegetation Index (NDVI), Version 5. Available online: <http://www.geodata.cn> (accessed on 21 September 2022).
45. Holben, N.B. Characteristics of maximum-value composite images from temporal AVHRR data. *Int. J. Remote Sens.* **1986**, *7*, 1417–1434. [[CrossRef](#)]
46. Fensholt, R.; Proud, S.R. Evaluation of earth observation based global long term vegetation trends—Comparing GIMMS and MODIS global NDVI time series. *Remote Sens. Environ.* **2012**, *119*, 131–147. [[CrossRef](#)]
47. Tian, F.; Fensholt, R.; Verbesselt, J.; Grogan, K.; Horion, S.; Wang, Y.J. Evaluating temporal consistency of long-term global NDVI datasets for trend analysis. *Remote Sens. Environ.* **2015**, *163*, 326–340. [[CrossRef](#)]
48. 1-km Monthly Mean Temperature Dataset for China (1901–2021). Available online: <http://data.tpdc.ac.cn/zh-hans/> (accessed on 22 August 2022).
49. Peng, S.Z.; Ding, Y.X.; Liu, W.Z.; Li, Z. 1 km monthly temperature and precipitation dataset for China from 1901 to 2017. *Earth Syst. Sci. Data* **2019**, *11*, 1931–1946. [[CrossRef](#)]
50. McColl, K.A. Practical and Theoretical Benefits of an Alternative to the Penman-Monteith Evapotranspiration Equation. *Water Resour. Res.* **2020**, *56*, e2020WR027106. [[CrossRef](#)]
51. Proutsos, N.D.; Tsiros, I.X.; Nastos, P.; Tsaousidis, A. A note on some uncertainties associated with Thornthwaite's aridity index introduced by using different potential evapotranspiration methods. *Atmos. Res.* **2021**, *260*, 105727. [[CrossRef](#)]
52. Hargreaves, G.H.; Allen, R.G. History and evaluation of Hargreaves evapotranspiration equation. *J. Irrig. Drain. Eng.* **2003**, *129*, 53–63. [[CrossRef](#)]
53. Su, Y.J.; Guo, Q.H.; Hu, T.Y.; Guan, H.C.; Jin, S.C.; An, S.Z.; Chen, X.L.; Guo, K.; Hao, Z.Q.; Hu, Y.M.; et al. An updated Vegetation Map of China (1:1000000). *Sci. Bull.* **2020**, *65*, 1125–1136. [[CrossRef](#)]
54. Wu, Z.H.; Huang, N.E. Ensemble empirical mode decomposition: A noise-assisted data analysis method. *Adv. Adapt. Data Anal.* **2009**, *1*, 1793. [[CrossRef](#)]
55. Lambert, J.; Drenou, C.; Denux, J.P.; Balent, G.; Cheret, V. Monitoring forest decline through remote sensing time series analysis. *Gisci. Remote Sens.* **2013**, *50*, 437–457.
56. Vicente-Serrano, S.M.; Begueria, S.; Lopez-Moreno, J.I. A Multiscalar Drought Index Sensitive to Global Warming: The Standardized Precipitation Evapotranspiration Index. *J. Clim.* **2010**, *23*, 1696–1718. [[CrossRef](#)]
57. Peng, J.; Wu, C.Y.; Zhang, X.Y.; Wang, X.Y.; Gonsamo, A. Satellite detection of cumulative and lagged effects of drought on autumn leaf senescence over the Northern Hemisphere. *Global Chang. Biol.* **2019**, *25*, 2174–2188. [[CrossRef](#)]
58. Jiang, S.S.; Chen, X.; Smettem, K.; Wang, T.J. Climate and land use influences on changing spatiotemporal patterns of mountain vegetation cover in southwest China. *Ecol. Indic.* **2021**, *121*, 107193. [[CrossRef](#)]
59. Martin, B.; Yue, Y.M.; Wigneron, J.P.; Tong, X.W.; Tian, F.; Jepsen, M.R.; Xiao, X.M.; Verger, A.; Mialin, A.; Al-Yaari, A.; et al. Satellite-observed Major Greening and Biomass Increase in South China Karst During Recent Decade. *Earth's Future* **2018**, *6*, 1017–1028.
60. Yang, H.; Hu, J.; Zhang, S.; Xiong, L.; Xu, Y. Climate Variations vs. Human Activities: Distinguishing the Relative Roles on Vegetation Dynamics in the Three Karst Provinces of Southwest China. *Front. Earth Sci.* **2022**, *10*, 799493. [[CrossRef](#)]

61. Chu, H.S.; Venevsky, S.; Wu, C.; Wang, M.H. NDVI-based vegetation dynamics and its response to climate changes at Amur-Heilongjiang River Basin from 1982 to 2015. *Sci. Total Environ.* **2018**, *650*, 2051–2062. [[CrossRef](#)]
62. Ding, Z.; Zheng, H.; Liu, Y.; Zeng, S.D.; Yu, P.J.; Shi, W.; Tang, X.G. Spatiotemporal Patterns of Ecosystem Restoration Activities and Their Effects on Changes in Terrestrial Gross Primary Production in Southwest China. *Remote Sens.* **2021**, *13*, 1209. [[CrossRef](#)]
63. Li, Y.J.; Ren, F.M.; Li, Y.P.; Wang, P.L.; Yan, H.M. Characteristics of the Regional Meteorological Drought Events in Southwest China During 1960–2010. *J. Meteorol. Res.* **2014**, *28*, 381–392. [[CrossRef](#)]
64. Wang, L.; Chen, W.; Zhou, W.; Huang, G. Understanding and detecting super-extreme droughts in Southwest China through an integrated approach and index. *Q. J. R. Meteorol. Soc.* **2016**, *142*, 529–535. [[CrossRef](#)]
65. Sun, H.; Wang, X.P.; Fan, D.Y.; Sun, O.J.X. Contrasting vegetation response to climate change between two monsoon regions in Southwest China: The roles of climate condition and vegetation height. *Sci. Total Environ.* **2021**, *802*, 149643. [[CrossRef](#)]
66. Li, G.; Li, C.Y.; Zhou, W.; Wen, B. Climatic Characteristics of Rainfall over Southwest China during Spring and Spring Months. *Clim. Environ. Res.* **2020**, *25*, 575–587.
67. Mei, S.L.; Chen, S.F.; Li, Y.; Aru, H. Interannual Variations of Rainfall in Late Spring over Southwest China and Associated Sea Surface Temperature and Atmospheric Circulation Anomalies. *Atmosphere* **2022**, *13*, 735. [[CrossRef](#)]
68. Zhang, L.; Xiao, J.F.; Li, J.; Wang, K.; Lei, L.P.; Guo, H.D. The 2010 spring drought reduced primary productivity in southwestern China. *Environ. Res. Lett.* **2012**, *7*, 045706. [[CrossRef](#)]
69. Lian, X.; Piao, S.L.; Li, L.Z.X.; Li, Y.; Huntingford, C.; Cuais, P.; Cescatti, A.; Janssens, I.A.; Penuela, J.; Buermann, W.; et al. Summer soil drying exacerbated by earlier spring greening of northern vegetation. *Sci. Adv.* **2020**, *6*, eaax0255. [[CrossRef](#)]
70. Xu, X.J.; Liu, H.Y.; Lin, Z.S.; Jiao, F.S.; Gong, H.B. Relationship of Abrupt Vegetation Change to Climate Change and Ecological Engineering with Multi-Timescale Analysis in the Karst Region, Southwest China. *Remote Sens.* **2019**, *11*, 1564. [[CrossRef](#)]
71. Vicente-Serrano, S.M.; Gouveia, C.; Camarero, J.J.; Begueria, S.; Trigo, R.; Lopez-Moreno, J.I.; Azorin-Molina, C.; Pasho, E.; Lorenzo-Lacruz, J.; Revuelto, J.; et al. Response of vegetation to drought time-scales across global land biomes. *Proc. Natl. Acad. Sci. USA* **2013**, *110*, 52–57. [[CrossRef](#)]
72. Yan, W.M.; Zhong, Y.Q.W.; Shangguan, Z.P. Responses of different physiological parameter thresholds to soil water availability in four plant species during prolonged drought. *Agric. Forest Meteorol.* **2017**, *247*, 311–319. [[CrossRef](#)]
73. Ma, Z.Q.; Guo, D.L.; Xu, X.L.; Lu, M.Z.; Bardgett, R.D.; Eissenstat, D.M.; McCormack, M.L.; Hedin, L.O. evolutionary history resolves global organization of root functional traits. *Nature* **2018**, *555*, 94–97. [[CrossRef](#)] [[PubMed](#)]
74. Chen, W.; Bai, S.; Zhao, H.M.; Han, X.R.; Li, L.H. Spatiotemporal analysis and potential impact factors of vegetation variation in the karst region of Southwest China. *Environ. Sci. Pollut. Res.* **2021**, *28*, 61258–61273. [[CrossRef](#)]

Disclaimer/Publisher’s Note: The statements, opinions and data contained in all publications are solely those of the individual author(s) and contributor(s) and not of MDPI and/or the editor(s). MDPI and/or the editor(s) disclaim responsibility for any injury to people or property resulting from any ideas, methods, instructions or products referred to in the content.